THE JOURNAL OF PHYSICAL CHEMISTRY C

Article

pubs.acs.org/JPCC

Tuning Electronic Properties of Monolayer Hexagonal Boron Phosphide with Group III–IV–V Dopants

Berk Onat,[†,‡] Lutfiye Hallioglu,[†,‡] Semran İpek,[†,§] and Engin Durgun*[,†,‡]

[†]UNAM-National Nanotechnology Research Center, Bilkent University, 06800 Ankara, Turkey

[‡]Institute of Materials Science and Nanotechnology, Bilkent University, 06800 Ankara, Turkey

[§]Department of Engineering Physics, Istanbul Medeniyet University, 34700, Göztepe-Istanbul, Turkey

Supporting Information

ABSTRACT: An extensive study on doping of two-dimensional (2D) hexagonal boron phosphide (*h*-BP) which is a direct band gap semiconductor was performed by using ab initio methods based on spin-polarized density functional theory. The interaction of group III–IV–V elements with *h*-BP is explored, considering both adsorption and substitution cases, and the resulting structural and electronic properties are examined. The variation of adsorption (substitution) energies and band gap values are systematically analyzed and trends are identified. Upon adsorption, the most of the elements bound on top of P atom forming dumbbell geometry which generates characteristic spin-polarized impurity states. The substitution of B or P by group III–IV–V elements can produce extra electrons/holes which lead to n-type and p-type doping for adequate cases. Additionally, doping can further generate impurity resonant states. Functionalization of *h*-BP with adatoms can tune the electronic structure and would be useful for nanoelectronic applications in low-dimensions.

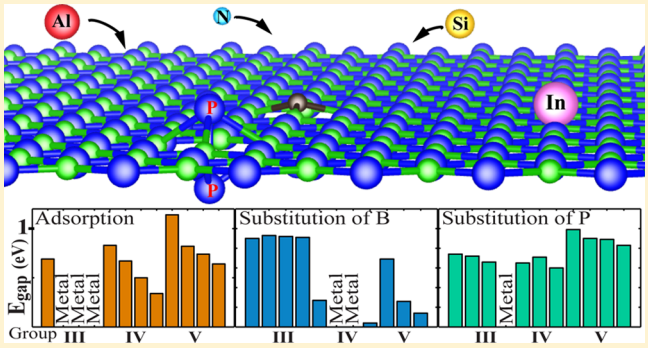

INTRODUCTION

Graphene has been the prominent two-dimensional (2D) material investigated in many theoretical and experimental studies owing to its remarkable properties such as massless Dirac Fermion-like charge carriers and half-integer quantum Hall effect.[1] While graphene is attributed as a promising candidate for many nanoelectronic applications because of its high conductivity and high carrier mobility (10^5 cm^2 V^{-1} s^{-1}),[2] the undesired on/off ratio with the lack of a fundamental band gap limits its applications in electronic devices. To find the counterpart of graphene in 2D structures with the desired electronic properties based on single elements and compounds has encouraged an active research field. The motivation has led to realize new 2D materials[3] including monoelement 2D systems (silicene,[4−6] germanene,[7] stanene,[8] phosphorene,[9] etc.), transition-metal dichalcogenides,[10−12] and transition metal carbide and carbon nitride based MXenes.[13] Additionally, many other 2D systems including hexagonal group V[14−17] and group II–VI,[18,19] III–V,[18] III–VI,[20−22] and group IV–IV,[18] IV–VI[23] compounds have been predicted theoretically, and some of them have already been synthesized.

Among these 2D systems, MoS_2 and phosphorene have taken more attraction in the field of nanoelectronics because of their direct band gaps (1.8 and 2.0 eV).[24−26] However, transistor applications of these semiconductors show that their carrier mobilities are not suitable enough for electronic and optoelectronic device manufacturing.[27,28] The need to find alternative 2D semiconductors with a direct and narrow band gap drive the interest to other systems such as III–V compounds. Following the successful epitaxial growth of few-layered AlN nanosheets on Ag(111) surface[29] and monolayer GaN via a migration-enhanced encapsulated growth technique utilizing epitaxial graphene,[30] monolayer boron–phosphide (*h*-BP) with its theoretical 0.9–1.36 eV direct band gap[31] is referred to be a potential candidate for advancing 2D devices.[26] Particularly, 2D materials with narrow band gaps can be used in field effect transistor (FET) applications at nanoscale,[32] thermoelectric applications,[33] and also nanoelectronic devices operated at near and far-infrared (IR) spectrum.[34]

Even not yet synthesized, *h*-BP has been predicted theoretically and ab initio studies suggest that it has stable, planar, hexagonal monolayer structure.[18,35,36] Monolayer boron–pnictogens (BP, BAs, and BSb) also show superior carrier mobilities (over 10^4 cm^2 V^{-1} s^{-1}) which is particularly comparable with high mobility of graphene.[26] Additionally Çakır et al. showed that n- and p-doped *h*-BP can serve as an ideal 2D p–n junction.[36] All these progressions have clearly showed that monolayer *h*-BP is a potential competitor in 2D materials beyond graphene. However, for electronic device

Received: October 12, 2016
Revised: January 24, 2017
Published: February 15, 2017

DOI: 10.1021/acs.jpcc.6b10334
J. Phys. Chem. C 2017, 121, 4583−4592

applications at nanoscale, controlling and modifying electronic properties has upmost importance.

Monolayer semiconductors can also be functionalized by doping which can significantly alter the electronic properties. Recently, it is shown that arsenene[37] and antimonene[38] allotropes can chemically absorb different elements and their electronic structures are substantially modified. Adsorption of adatoms can also change the local atomic configuration of the host system depending on their binding sites. For instance, group IV atoms adsorbed on silicene, germanene, and stanene can exothermically form dumbbell (DB) structures leading to new electronic properties depending on the type of the adatom.[39]

In the present work, we performed an extensive study on interactions of adatoms with *h*-BP by using first-principle techniques. The alteration of structural and electronic properties are explored with doping (adsorption and substitution) considering group III (B, Al, Ga, and In), group IV (C, Si, Ge, and Sn), and group V (N, P, As, and Sb) elements. To determine the ground state configurations, we examined all the possible sites for adsorption and substitution. It is found that the most favorable binding site for adsorption is on top of P atom except for Al, Ga, and In. This bonding results in DB formation which generates spin-polarized impurity states. The variation of adsorption (substitution) energies and band gap values is systematically analyzed and trends are correlated with relevant parameters including electronegativity, bonding distance, and radius of atoms. The resulting electronic structures upon doping show wide variety of electronic and magnetic properties differing from pristine *h*-BP which would be useful for highly desired nanoscale electronic and optical applications.

COMPUTATIONAL DETAILS

We have carried out first-principles calculations based on spin-polarized density functional theory (DFT)[40,41] by using the Vienna ab initio simulation package (VASP).[42] Projector augmented-wave potentials (PAW) are used to define the considered elements and the exchange-correlation is approximated with Perdew–Burke–Ernzerhof (PBE) functional in generalized gradient approximation (GGA).[43] van der Waals (vdW) interactions are found to have an importance in determining the stability and correcting the formation energies of impurities in semiconductors.[44] To better determine the adsorption and substitution energies of dopants, we include vdW corrections using Grimme method (DFT-D2).[45] A plane wave basis set is chosen with a kinetic energy cutoff of 500 eV. The atomic positions are optimized using conjugate gradient method in consecutive steps of energy and force minimizations. The energy convergence is ensured with 10^{-5} eV tolerance and a maximum force of 0.002 eV/Å is allowed on each atom. We also apply Heyd–Scuseria–Ernzerhorf (HSE06) hybrid functionals[46] for the corrected electronic structure. The HSE06 functional is constructed by mixing 25% of the Fock exchange with 75% of the PBE exchange and 100% of the PBE correlation. The HSE06 functional has proved to be a successful method to estimate the band gaps of 2D semiconductors.[14,32,47,48]

When the dopant is introduced in the vicinity of a bare *h*-BP, two possible cases can be considered: adsorption of the adatom at an available site on the surface and substitution of B or P atoms with the dopant. Both of the cases are modeled using a supercell that is constructed with $n \times n$ primitive cells (see Figure 1). We consider supercells from $n = 1$ to $n = 7$ and select a 5×5 supercell which is suitable to obtain impurity states with minute interactions of adatoms at periodic images. In our tests, we find that the highest difference in binding energy of the selected cases are below 50 meV between 5×5 and 6×6 supercells. The Brillouin zone (BZ) is sampled with the Monkhorst–Pack scheme[49] with $5 \times 5 \times 1$ *k*-point mesh which yields well-converged results for 5×5 supercell.

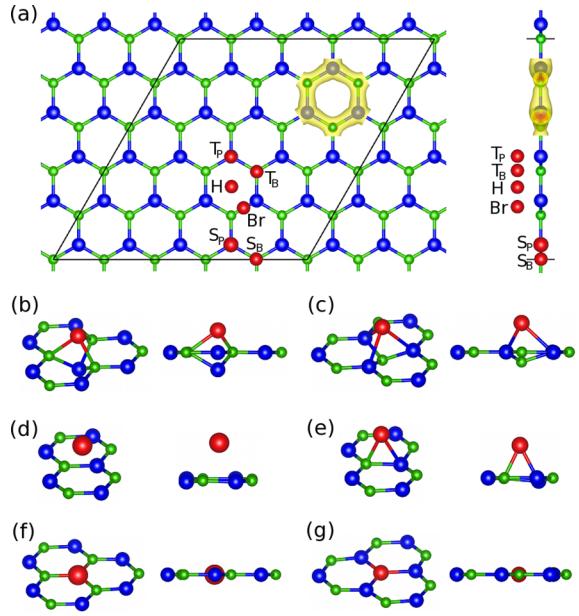

Figure 1. (a) Top (left) and side (right) views of the 5×5 supercell of monolayer *h*-BP. Inset shows the total charge density distribution of a hexagon in pristine *h*-BP. The adsorption and substitution sites are indicated with *H*, *Br*, T_P, T_B, S_P, and S_B labels. The dopant, B, snd P atoms are shown with red, green, and blue spheres, respectively. The local atomic reconfigurations (perspective and side views) of adatom adsorption (b) on T_P, (c) on T_B, (d) on *H*, and (e) on *Br* sites and adatom substitution with (f) B and (g) P.

To determine the adsorption energies of adatoms, we used the binding energy definition: $E_b = E(h\text{-BP}) + E(\text{X}) - E(h\text{-BP+X})$, where $E(h\text{-BP})$ is the total energy of pristine monolayer *h*-BP, $E(\text{X})$ is the energy of single adatom in vacuum, and $E(h\text{-BP+X})$ is the energy of the final optimized structure after adsorption. Similarly, the substitution energy is calculated using the definition $E_s = E(h\text{-BP}) + E(\text{X}) - E(h\text{-BP+X}) - E(\text{B/P})$ where $E(h\text{-BP+X})$ denotes the energy of the structure with an impurity atom at S_B/S_P sites and $E(\text{B/P})$ refers to the single atom energy of B or P that is substituted. The charge on each atom after adsorption (substitution) is determined with Bader analysis. After the self-consistent calculation, the excess charge on the adatom, δ, is calculated by subtracting the Bader charge of the adatom, ρ_A from the initial valence charge, Z_A of the atom at vacuum using the equation $\delta = Z_A - \rho_A$. Accordingly, $\delta < 0$ implies the excess electron charge that is localized at the adatom site. To identify the nature of the variation in E_b, E_s, and δ (and also the band gap) with the dopant type, we consider an extensive set of parameters: nearest neighbor bond-length and atomic charge in the doped *h*-BP and electron negativity, electron affinity, atomic radius, ionization energies, and elastic constants of the doping elements.

Structural stability of the doped h-BP is analyzed by investigating the vibrational modes of the resulting geometries. The phonon dispersion and hence the vibrational modes of the

DOI: 10.1021/acs.jpcc.6b10334
J. Phys. Chem. C 2017, 121, 4583–4592

Table 1. Structural, Electronic, and Magnetic Properties of *h*-BP upon Adsorption of Adatoms[a]

adatom	site	d_{nn} (Å)	d_P (Å)	E_b (eV)	E_g(ML) (eV)	E_g(IM) (eV)	ΔE (meV)	μ (μ_B)	δ
B	T_P	1.75	1.65	3.57	1.13	0.69	10	1.00	0.11
Al	H	2.69	2.80	1.90	1.18	0.0	∼0	0.00	0.75
Ga	H	2.76	2.83	1.80	1.19	0.0	∼0	0.00	0.43
In	H	2.94	3.00	1.54	1.21	0.0	∼0	0.00	0.57
C	T_P	1.54	1.86	4.82	1.10	0.83	86	2.02	−1.97
Si	T_P	2.07	2.29	2.94	1.13	0.67	31	1.82	0.87
Ge	T_P	2.25	2.41	2.33	1.09	0.50	56	1.85	0.45
Sn	T_P	2.48	2.60	1.92	1.09	0.34	36	1.88	0.60
N	T_P	1.55	1.89	2.56	1.39	1.14	15	1.09	−1.99
P	T_P	1.95	2.23	2.36	1.27	0.82	16	1.10	−0.12
As	T_P	2.11	2.36	1.70	1.20	0.74	16	1.10	−1.16
Sb	T_P	2.34	2.54	1.21	1.15	0.64	18	1.10	0.50

[a]Adatom type, site, bonding distances to nearest neighbor B and P atoms (d_{nn} and d_P), binding energies (E_b), band gaps (E_g(ML) and E_g(IM)), the energy differences between spin-polarized and unpolarized calculations (ΔE), magnetic moment per unitcell (μ_B), and the atomic charges (δ) are tabulated.

doped *h*-BP are calculated using the PHONOPY package,[50] and the force constants of the relaxed structures are determined using linear response theory within the density functional perturbation theory (DFPT)[51,52] implemented in VASP.

RESULTS AND DISCUSSION

Atomic Structure and Energetics. We carry-out structural optimization calculations to find the lowest energy configuration of *h*-BP and find that the system is planar with an optimized lattice constant of 3.21 Å in agreement with previous studies.[18,36] Monolayer *h*-BP has σ bonds between B and P atoms with 3-fold symmetries and sp^2 hybridization stabilizes the honeycomb structure. This electronic configuration leads to unoccupied p_z orbital for B and lone pair of electrons at p_z orbital of P. The resulting off-balanced electron distribution between B and P atoms with an additional electron charge on P atoms can be seen from the charge density isosurfaces in Figure 1a. Following the optimization of pristine 5 × 5 *h*-BP, we analyze the possible adsorption sites for group III, IV, and V adatoms. We determine four possible sites on the hexagonal sheet that are labeled with *H*, *Br*, T_P, and T_B indicating hollow, bridge, top site on P, and top site on B atoms. In Figure 1, the adsorption sites are shown together with the representative final local atomic configurations. As it is demonstrated in early studies,[39] the adsorption of adatom can push one of the lattice atoms downward which leads to a dumbbell (DB) formation. The DB phase is studied in detail for 2D group IV systems.[39,53,54] Our results indicate that the most favorable configuration for adsorption is the DB formation on top of P (DP_P) for all cases except for Al, Ga and In. Contrary to other elements, Al, Ga, and In prefer binding site *H* but the energy difference between *H* and T_P is not high (∼0.1 eV) indicating the possibility of DB formation for these elements as well. We also find that not all adsorption sites are stable for the considered elements. For instance, none of the group IV elements can form a stable configuration at *Br*. Similarly, B can not be adsorbed at *H* site and Sb does not bind at the *Br* site. Both B and Sb move to the T_P site without facing an energy barrier. Interestingly, there are only two adsorption sites for N: *Br* and T_P. All other initial adsorption configurations end up at the *Br* site with a substantial buckling of *h*-BP after relaxation.

Taking possibility of buckling into account, we consider adsorption of N as a representative system and checked whether planar geometry of *h*-BP is preserved upon doping. Carrying out linear response calculations with DFPT, we calculated phonon dispersions of N adsorptions at *Br* and T_P sites. The results show that while the planar geometry with formation of DB at T_P is stable, the adsorption at *Br* resulting in buckled geometry is not stable with the negative frequency modes (Figure S1, Supporting Information). The calculations are also repeated with larger supercell (7 × 7) for specific cases in order to eliminate possible size constraint effects and ground state configurations are confirmed.

The obtained structural, electronic, and magnetic properties are summarized in Table 1. Upon interaction of group III−IV−V elements, the bonding at the T_P site substantially changes. Mainly p-orbitals of both adatom and P contribute to new covalent bonding formation. Introducing the fourth bond with P in DB geometry rearranges the electronic configuration with a tetragonal symmetry in the structure. Adatom forms weak 3-fold coordinated bonds with the nearest host B atoms on-top of the host P atom and have more sp^3-like hybridization. The resulting DB_P formations for all cases are provided in Figure S2, Supporting Information. Adatoms with a smaller atomic radius (*R*) push the host P atom more. Even there, C and N almost substitute P and form nearly planar bonds with B atoms. The variation of bonding distance (d_{nn} where *nn* represents the bonding between the atom and the nearest neighbor atoms) and the distance between the adatom and the host P atom (d_P) are also related to *R* and both increase when going down in a group. On the other hand d_{nn} and d_P do not vary along a row, which indicates that bonding geometry is correlated with the size and not directly with the valency.

The net atomic charges (δ) on each adatom after adsorption are given in Table 1. While C, N, P, and As accept electrons from *h*-BP, the other elements donate electrons. The variation of δ within each group is not simple and depends on the *R*, electron affinity (κ) and electron negativity (χ) as shown in Figure 2b.

Finally, our results indicate that while d_{nn} increases when moving down in a group, the adsorption energies, E_b decrease. This is the expected weakening in binding with the increase of the bond length. Our analysis shows that the variation of E_b is highly correlated with d_{nn} and χ of the dopants as illustrated in Figure 2a. The plot of χ/d_{nn} and E_b with respect to elements in a group follow a similar trend.

DOI: 10.1021/acs.jpcc.6b10334
J. Phys. Chem. C 2017, 121, 4583−4592

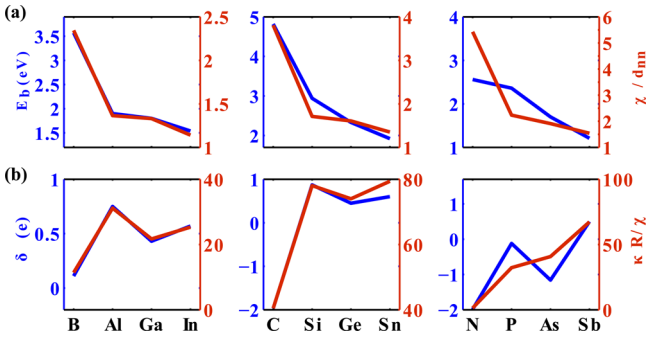

Figure 2. (a) Variation of binding energy (E_b) and (b) the atomic charge (δ) with respect to group III–IV–V elements. The trends are compared with the variation of atomic radius (R), bonding distance (d_{nn}), electron affinity (κ) and electronegativity (χ).

To provide a comprehensive analysis on doping of h-BP, we also investigate substitutions of B and P atoms with all the considered elements. Substitutions in general do not result in any deformation and the planar geometry is preserved. The typical relaxed geometries upon substitutions at lattice sites S_B of B and S_P of P atoms are shown in Figure 1, parts f and g. The lattice distortions upon substitutions are local and only the bond distances between the impurities and nearby atoms change. When the substitution energies, E_S are examined (in Table 2), only the substitutions of P with C and N are found exothermic reactions and all other cases requires energy. It is likely that the substitutions of P atoms can take place spontaneously upon the existence of C and N atoms in the vicinity of h-BP. For all other elements, E_S is negative and its absolute value increases for both B and P substitutions when moving down in each group. Similar to the adsorption case, variation of E_S is correlated with d_{nn} (or R) of each element. The Bader charge analyses reveal that variation of δ on dopants are directly proportional with χ and inversely proportional with R of the substitute elements. The plot of the trends are provided in the Figure S3, Supporting Information.

Electronic and Magnetic Properties. In this section, the electronic and magnetic properties of doped h-BP are investigated for both the adsorption and substitution cases. Adsorption in general leads to spin-polarized impurity states which are mainly contributed by p-orbitals of the atoms in impurity region (IM). While IM consists of the dopant and its first and second nearest neighbors, the rest of the h-BP lattice is referred monolayer region (ML) in present study. In Figure 3, we present the band structures of h-BP upon adsorption with group III–IV–V elements together with their total (DOS) and partial (PDOS) density of states. In PDOS, the contributions from s and p orbitals of the IM are taken into account. The bands, DOS, and PDOS are colored accordingly. If the majority of the contributions to a band is from IM, the same color code is used for that band and the PDOS. The band gap of h-BP (E_g(ML)) is defined as the difference between the valence band maximum (VBM) and conduction band minimum (CBM) and is shown with a background color in Figure 3 for better illustration. The band gap of the IM region (E_g(IM)) is defined as the difference between the average energy of localized impurity bands and CBM.[55]

When electronic band structures are classified by groups, we reveal that group III elements except B, prefer binding to the H site, and the ground state configuration is metallic without spin-polarized impurity states. Al, Ga, and In donate charge to the h-BP, resulting in a positive δ charge on adsorbed atoms (Table 1), but the transferred charge is not localized in the IM region and disperse along the h-BP. Al, Ga, and In doping transforms the semiconducting system into metal (Figure 3). This characteristic change can be attributed to relatively low electronegativity χ of these three elements which are on average 18% smaller than the χ of pristine h-BP. While these adatoms prefer binding at H site, the energy difference between this site and T_P site is considerably small (~0.1 eV), so we analyze the band structures for the T_P configuration that forms DB phase as well. For both H and T_P cases, the electronic structures have similar profiles and the systems have metallic character. The band structures belonging to DB geometry are presented in Figure S4, Supporting Information. The remaining group III element, B, favors the T_P site to bind and forms an asymmetric DB upon adsorption. The bonds between adatom B and the host B atoms have sp^2-like hybridization due to an in-plane settlement. In this arrangement, host P atom, which is pushed down to form DB phase has sp^3-like hybridization and have 4-fold bonding with nearest four B atoms including the adsorbed one. Three valence electrons of dopant involve in bonding and the resulting system is a semiconductor with four localized and spin-polarized bands belonging to IM states. Only one of the spin-up band is occupied resulting in 1 μ_0 net magnetic moment.

All group IV elements prefer the T_P site and form DB geometry. The band structures are spin-polarized with localized IM states which is a characteristic feature of DB formation.[39] This is due to the occupation and hybridization of p orbitals in the structure upon adsorption. Differing from the case for group III elements, four valence electron of adatom take part in bonding. All spin-up IM states are filled and Fermi level splits the spin up and down IM states resulting in ~2 μ_0 magnetic moment. Adsorption of group IV elements not only induces impurity states but also modifies the band structure of pristine h-BP. The band gap of bare h-BP (E_g(ML)) increases from 0.9

Table 2. Substitution Energies, E_S, Band Gaps, $E_g(S_X)$ (X = P/B) and E_g(ML), and Atomic Charges (δ) for h-BP upon Substitutions of P and B with Selected Elements

substitute	property	Al	Ga	In	C	Si	Ge	Sn	N	As	Sb
B	E_s (eV)	−4.07	−4.69	−7.91	−0.46	−4.16	−5.67	−7.74	−3.67	−7.34	−9.29
	E_g(ML) (eV)	0.93	0.92	0.91	1.31	1.31	1.31	1.29	1.12	1.10	1.07
	$E_g(S_B)$ (eV)	0.93	0.92	0.91	0.27	–	–	–	0.69	0.26	0.14
	δ	2.01	0.69	0.65	−1.53	1.82	0.48	0.78	−1.69	−0.06	0.34
P	E_s (eV)	−2.70	−3.34	−5.81	3.00	−0.71	−1.97	−3.84	2.13	−1.40	−3.28
	E_g(ML) (eV)	1.16	1.17	1.04	0.97	1.22	1.25	1.25	0.99	0.89	0.83
	$E_g(S_P)$ (eV)	0.74	0.72	0.66	–	0.65	0.71	0.60	0.99	0.89	0.83
	δ	1.99	0.54	0.48	−1.96	1.68	0.49	0.50	−2.00	−0.17	0.39

DOI: 10.1021/acs.jpcc.6b10334
J. Phys. Chem. C 2017, 121, 4583–4592

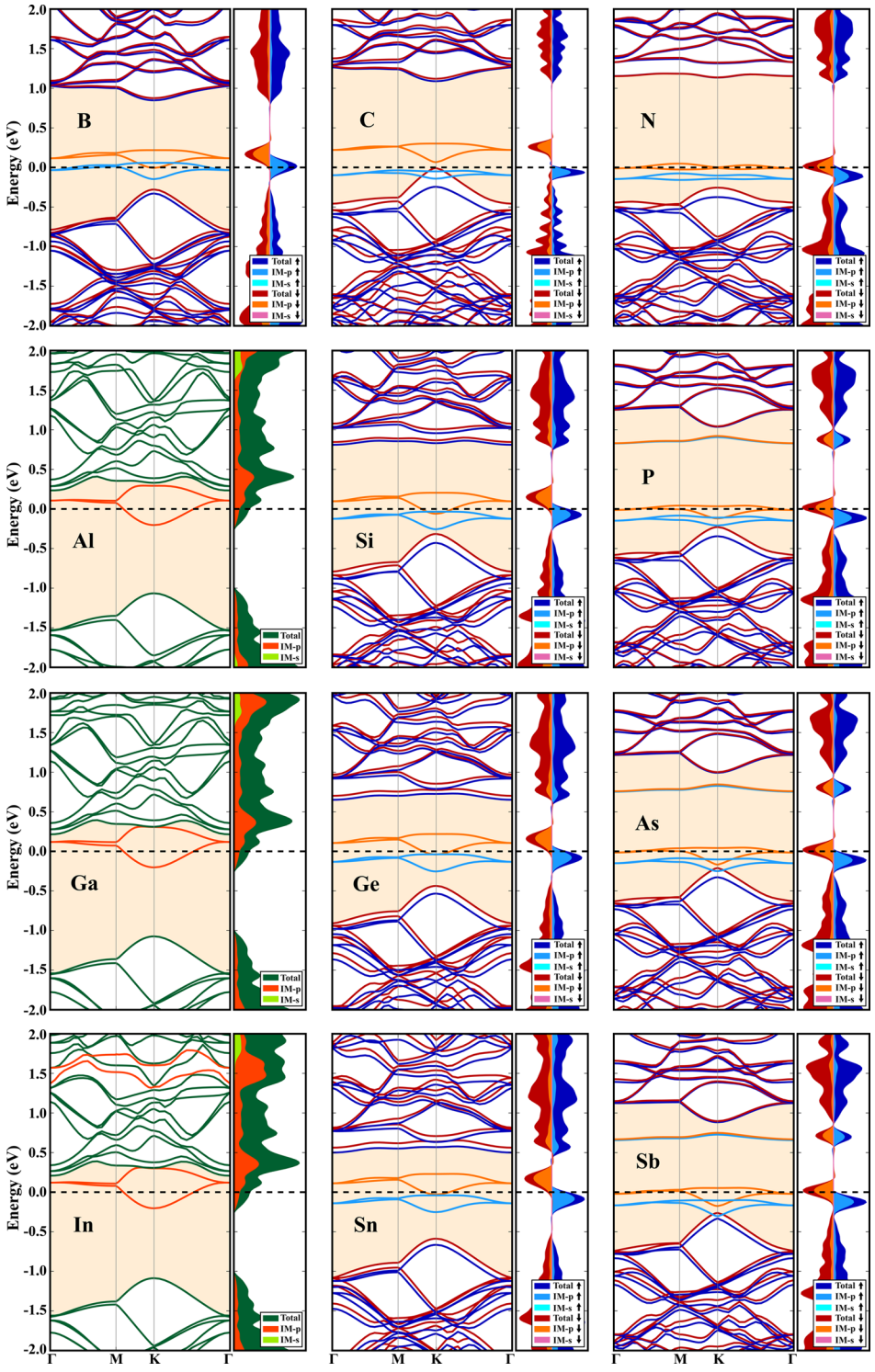

Figure 3. Electronic band structure, partial density of states (PDOS) of impurity region (IM), and total density of states (DOS) of *h*-BP upon adsorption of group III−IV−V adatom.

to ∼1.1 eV upon doping and this increase does not depend on the dopant type. On the other hand IM states shift up to CBM, decreasing the E_g(IM) when moving down in the group as shown in Figure 6. Interestingly for C adsorption, occupied spin-up impurity states lie inside the valence band and p orbital contributions of IM coincide with the states of *h*-BP at VBM. The impurity states clearly overlap with the host *h*-BP states just below VBM and indicate that the IM states of C adsorption have a significant nature of resonance impurity states (or virtual bound states).[56−58] While the states have the origin of hybridization between p orbitals of dopant and host atoms, they do not possess a deep and shallow impurity states but provide impurity resonance states of p-type doping. This may increase the overall hole concentration at the local impurity region caused by C doping. The electrons resonate at similar energies at electronic states of VBM and dopant which may lead the electrons to act like nearly free-electrons. These features have noticeable impact on the energy and charge

DOI: 10.1021/acs.jpcc.6b10334
J. Phys. Chem. C 2017, 121, 4583−4592

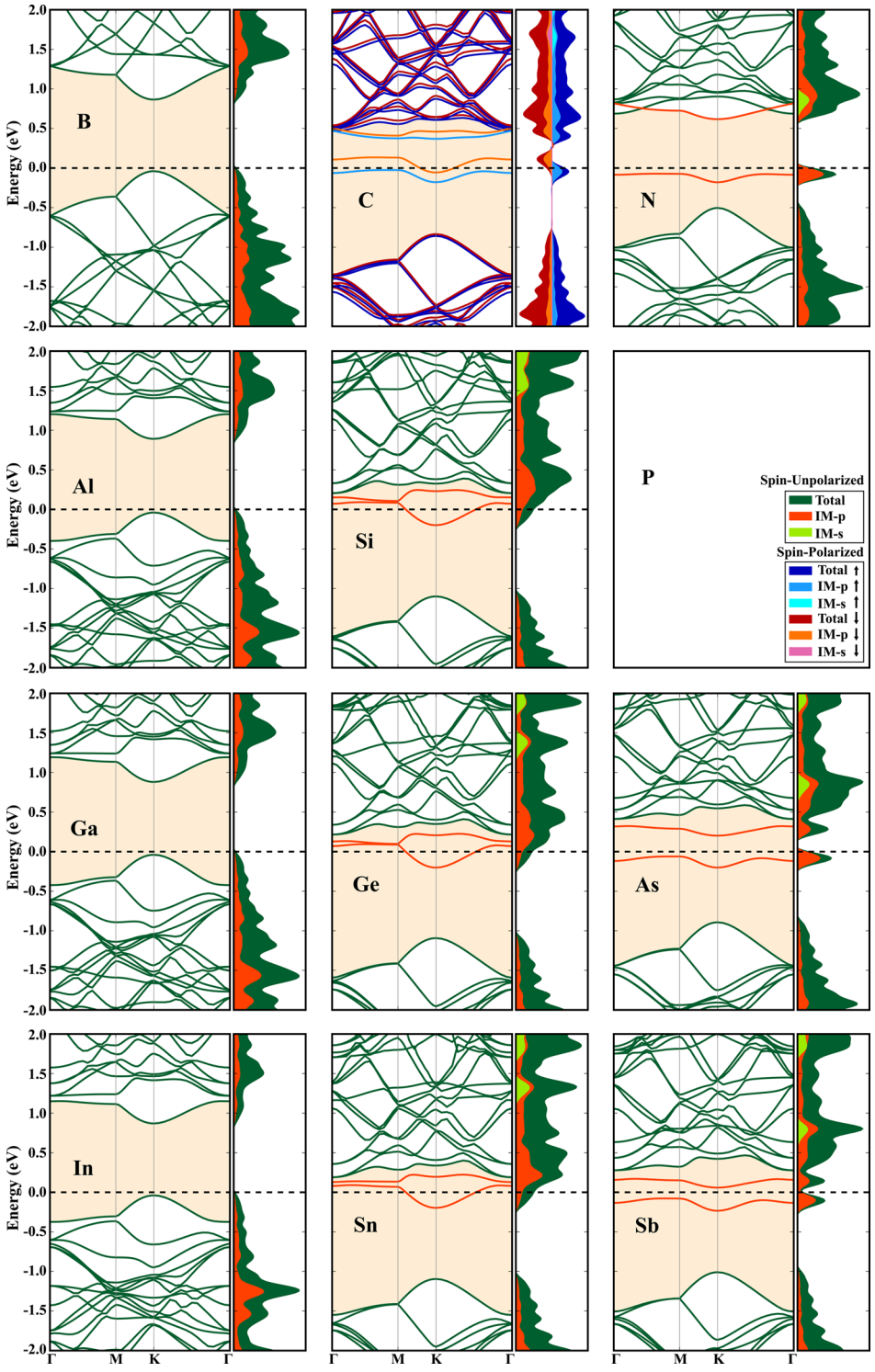

Figure 4. Electronic band structure, partial density of states (PDOS) of impurity region (IM), and total density of states (DOS) of *h*-BP upon substitution of B atom with group III–IV–V adatoms.

transfers and may enhance thermoelectric properties of the material.[57]

Similar to the case for group IV, all adatoms in group V prefer the T_P site forming DB geometry, and spin-polarized IM states are obtained. As there are five valence electrons, all spin-up IM states are occupied and Fermi level splits the spin-down IM states resulting in ∼1 μ_0 magnetic moment. Differing from the other groups, breaking of the sp^2 bonds in favor of sp^3-like hybridization for tetragonal symmetry initiates an additional impurity level closer to the CBM because of the occupation at p_z orbital of P host and adsorbent. E_g(ML) increases to 1.39 eV upon adsorption of N but decreases gradually to 1.15 eV for the case of Sb. Following a similar trend in adsorption of group III elements, E_g(IM) also decreases when moving down in the group. Similar to the impurity states of C doping, As and Sb show impurity band states overlapping with the states just below VBM. However, in these two cases, the states may not

DOI: 10.1021/acs.jpcc.6b10334
J. Phys. Chem. C 2017, 121, 4583−4592

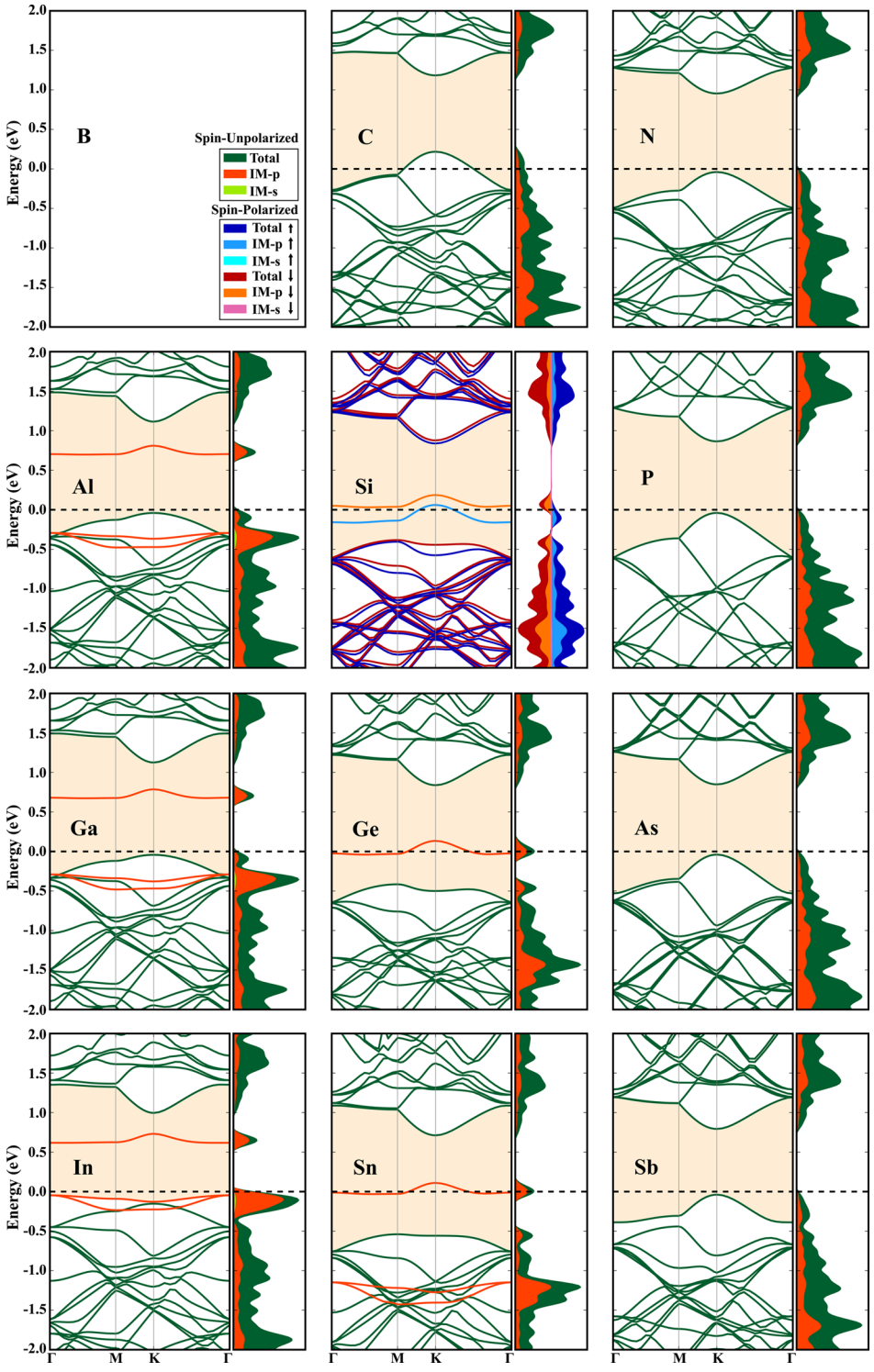

Figure 5. Electronic band structure, partial density of states (PDOS) of impurity region (IM), and total density of states (DOS) of *h*-BP upon substitution of P atom with group III–IV–V adatoms.

have a resonant origin since the PDOS of the impurity states do not coincide with DOS of host *h*-BP.

When compared, for all groups, the impurity originated band gaps are highly correlated with the structural changes which are driven with the bonding distances and also with the differences in χ between the substrate and adatoms. As shown in Figure 6a, the change of E_g(IM) upon adsorption and the variation of χ/d_{nn} with respect to the type of elements in each group follow a similar pattern. Similar analysis can be performed for each row, and it is found that E_g(IM) increases when moving along a row (given in Table 1).

Finally, in Table 1, we present the magnetization, $\mu(\mu_\beta)$ of the supercell. The magnetic moment is ∼1 μ_0 for group III (only for B), group V elements and ∼2 μ_0 for group IV elements correlated with the occupancy of impurity states. However, when the energy differences between spin polarized and unpolarized states (ΔE^{un-sp}) are calculated, it is revealed that ΔE is very small (below 100 meV) which indicates that the

DOI: 10.1021/acs.jpcc.6b10334
J. Phys. Chem. C 2017, 121, 4583−4592

spin polarization is likely to be observed only at low temperatures.

For substitution, we considered the cases where B (or P) is replaced by group III−IV−V elements excluding the substitution of B with P or vice versa. The resulting band structures are presented in Figure 4 and Figure 5 and band gaps are reported in Table 2. The band structure of pristine *h*-BP with the same supercell size is also included to provide a complete comparison.

When B atom is substituted with the selected elements, we find the following results: substitutions of B with group III elements do not introduce additional electrons/holes hence no impurity states are generated. Moreover, changing the element type has only minute effect on the valence and conduction bands and E_g(ML) of pristine *h*-BP is preserved. On the other hand substitutions with group IV provide an additional electron and the systems become metallic except for C. For the cases of Si, Ge, and Sn, new bands arise as shown in Figure 4 but PDOS analyses indicate that these bands do not only have impurity origin and IM states are dispersive. Accordingly, n-type character can not be justified. On the other hand, for the case of C, spin-polarized IM states below CBM are obtained and the system becomes an n-type semiconductor. This can be attributed to the size match of C with B (bond distances are 1.54 Å for C and 1.56 Å for B, respectively) resulting in no local deformation, which can alters bonding and hence the electronic states of IM. In addition, 2p orbitals hybridize with 3p-orbitals of P in both cases. It should be noted that energy difference between spin-polarized and unpolarized states is below 10 meV indicating a nonmagnetic profile at ambient conditions. For group V elements, the systems become n-type semiconductor with generation of two IM states. Except for N, both IM states are below CBM but only one of them is occupied. This leads to n-type doping that is originated from the s-p hybridization in IM states. For the case of N, the PDOS profile in Figure 4 indicates a possible formation of resonance impurity states at conduction band with more delocalized features of IM.[56−58] Similar to the impurity states of C adsorption below VBM (Figure 3), here N substitution leads to resonance impurity states at CBM that coincide with the electronic states of substrate *h*-BP. In addition, the impurity levels are separated and the state closer to Fermi level shifts toward the valence band because of the high χ of N. As a summary, n-type doping with varying band gap can be obtained for substitutions of B with C, N, As and Sb. The variation of E_g(IM) is directly proportional with χ and inversely proportional with R (or d_{nn}) for all cases similar to adsorption and the trends are shown in Figure 6b.

An overall analysis on the band structures of the doped *h*-BP upon the substitution of P portrays the following results (in Figure 5): Substitution of P with group III elements generates occupied IM levels in valence band and also additional unoccupied level below CBM. The occupied IM levels in valence band show deep defect states for Al and Ga with the majority of contribution to PDOS from the impurity states.[56−58] For the case of In, however, the IM states coincide with the states of *h*-BP at valence band edge. The p orbital hybridization of In and nearest B atoms in IM and localized states of IM at valence band edge suggests that these states are resonance impurity states of p-type doping rather than deep defect states as in Al and Ga. For group IV elements, occupied and localized IM levels are obtained above VBM except for C. IM levels shift up to CBM when moving down in the group.

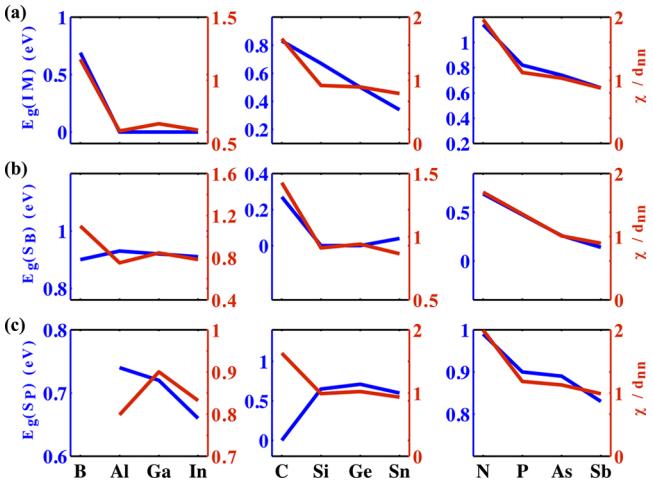

Figure 6. Variation of band gaps (a) E_g(DB), (b) E_g(S_B), and (c) E_g(S_P) with respect to respect to group III−IV−V dopants. The trends are compared with the variation of bonding distance (d_{nn}) and electronegativity (χ).

Interestingly, addition of C makes system metallic and no IM states are generated. This can be linked with high χ of C. Similar to the substitution of B with C, the substitution of P with Si results in spin-polarized IM states and p-type doping character is obtained. This is due to the matching bond distance (1.86 Å for Si and 1.87 Å for P) which preserves the symmetry of hexagonal BP structure with small structural distortions while providing additional hole at the p orbitals. For the case group V elements, there are no additional holes/electrons, thus no IM states are generated. E_g(ML) increases and becomes 0.99 eV for the case of N and then decreases gradually to 0.83 eV for Sb.

It can be concluded that, for both substitution of B and P cases, E_g(IM) decreases in parallel with the change of χ and with increase of the d_{nn} of the dopant when moving down in a group. These trends are presented in Figure 6 parts b and c.

As the band gaps are underestimated within standard GGA calculations, we recalculated band structures with hybrid functional method for selected cases to check whether our conclusions are valid. The obtained results for Ga, Ge, and As adsorptions on *h*-BP are presented in Figure S5, Supporting Information. To sum up, HSE06 results confirm the metallic state for Ga and thus for group III elements (except B). For Ge, characteristic spin-up and spin-down DB impurity states are obtained but they are clearly separated. The occupied states are settled at Fermi level while the unoccupied spin down states shift upward. Both E_g(ML) and E_g(IM) increase and become 1.52 and 0.71 eV, respectively. The electronic structure of As obtained with HSE06 calculations shows an additional feature. When HSE correction is included, the degenerate spin polarized impurity states split at Fermi level. This can be explained by the Jahn−Teller distortion[59] around the impurity atom. Since As has more sp^3-like hybridization bonding in *h*-BP upon adsorption, p orbital states do not have 3-fold degeneracy of hexagonal structure. In this case, the "spatial symmetry breaking"[59−61] is observed and levels are separated.

CONCLUSION

In conclusion, we investigated the structural and electronic properties of *h*-BP doped with selected atoms from group III−IV−V. We found that all elements except Al, Ga and In favor on top P atom as adsorption site and exothermically form DB

DOI: 10.1021/acs.jpcc.6b10334
J. Phys. Chem. C 2017, 121, 4583−4592

geometry. Al, Ga and In elements bound to hollow site, however the energy difference between the lowest energy configuration and T_P is very small suggesting the possibility of DB formation for those cases as well. Upon adsorption, semiconductor *h*-BP can become a metal (with group III) or spin-polarized semiconductor with varying band gap. The substitution of B or P with group III−IV−V elements can also modify the electronic structure without changing the planar structure. The system can be n- (B substituted with C, N, As, Sb) or p-type (P substituted with In, Si, Ge, Sb) semiconductor for suitable cases. Doping can further generate impurity resonant states. When the substitution energies are examined, only the substitutions of P with C and N are found exothermic reactions, thus can form BN and BC networks in *h*-BP and all other cases requires energy. Our results indicate that the modifications in electronic structure, especially the variation of band gap upon adsorption/substitution, are not only correlated with valency of adatoms but also depend on the size of dopant and final geometry after doping. Possibility of functionalization of *h*-BP by doping, which allows tuning electronic structure substantially, would be useful for highly desired nanoscale electronic and optical applications. With the tuning of its narrow band gap, *h*-BP can be one of the candidate 2D materials for various applications such as FETs at nanoscales, thermoelectric materials, and IR optical nanodevices.

■ ASSOCIATED CONTENT

Supporting Information

The Supporting Information is available free of charge on the ACS Publications website at DOI: 10.1021/acs.jpcc.6b10334.

Phonon dispersions and the related negative frequency mode for h-BP upon N adsorption at Br site and with DB_P phase, DB_P dumbbell formations upon adsorption of group III−IV−V elements, Bader charge profiles for substitution of B and P atoms by group III−IV−V elements, electronic band structure of DB_P phase for Al, Ga, and In adsorptions, and band structures of Ga, Ge, and As with HSE06 calculations (PDF)

■ AUTHOR INFORMATION

Corresponding Author

*(E.D.) E-mail: durgun@unam.bilkent.edu.tr.

ORCID

Engin Durgun: 0000-0002-0639-5862

Notes

The authors declare no competing financial interest.

■ ACKNOWLEDGMENTS

This work was supported by the Scientific and Technological Research Council of Turkey (TUBITAK) under Project No 113T050. The computing resources are provided by TUBITAK ULAKBIM—High Performance and Grid Computing Center (TR-Grid e-Infrastructure) and the National Center for High Performance Computing of Turkey (UHeM) under grant number 5003622015. E.D. acknowledges support from The Turkish Academy of Sciences within Outstanding Young Scientists Award Program (TUBA-GEBIP).

■ REFERENCES

(1) Zhang, Y.; Tan, Y.-W.; Stormer, H. L.; Kim, P. Experimental Observation of the Quantum Hall Effect and Berry's Phase in Graphene. *Nature* **2005**, *438*, 201−204.

(2) Long, M.-Q.; Tang, L.; Wang, D.; Wang, L.; Shuai, Z. Theoretical Predictions of Size-Dependent Carrier Mobility and Polarity in Graphene. *J. Am. Chem. Soc.* **2009**, *131*, 17728−17729.

(3) Bhimanapati, G. R.; Lin, Z.; Meunier, V.; Jung, Y.; Cha, J.; Das, S.; Xiao, D.; Son, Y.; Strano, M. S.; Cooper, V. R.; et al. Recent Advances in Two-Dimensional Materials Beyond Graphene. *ACS Nano* **2015**, *9*, 11509−11539.

(4) Vogt, P.; De Padova, P.; Quaresima, C.; Avila, J.; Frantzeskakis, E.; Asensio, M. C.; Resta, A.; Ealet, B.; Le Lay, G. Silicene: Compelling Experimental Evidence for Graphenelike Two-Dimensional Silicon. *Phys. Rev. Lett.* **2012**, *108*, 155501.

(5) Durgun, E.; Tongay, S.; Çıracı, S. Silicon and III-V Compound Nanotubes: Structural and Electronic Properties. *Phys. Rev. B: Condens. Matter Mater. Phys.* **2005**, *72*, 075420.

(6) Cahangirov, S.; Topsakal, M.; Aktürk, E.; Şahin, H.; Çıracı, S. Two- and One-Dimensional Honeycomb Structures of Silicon and Germanium. *Phys. Rev. Lett.* **2009**, *102*, 236804.

(7) Dávila, M.; Xian, L.; Cahangirov, S.; Rubio, A.; Le Lay, G. Germanene: A Novel Two-Dimensional Germanium Allotrope Akin to Graphene and Silicene. *New J. Phys.* **2014**, *16*, 095002.

(8) Zhu, F.-F.; Chen, W.-J.; Xu, Y.; Gao, C.-L.; Guan, D.-D.; Liu, C.-H.; Qian, D.; Zhang, S.-C.; Jia, J.-F. Epitaxial Growth of Two-Dimensional Stanene. *Nat. Mater.* **2015**, *14*, 1020.

(9) Li, L.; Yu, Y.; Ye, G. J.; Ge, Q.; Ou, X.; Wu, H.; Feng, D.; Chen, X. H.; Zhang, Y. Black Phosphorus Field-Effect Transistors. *Nat. Nanotechnol.* **2014**, *9*, 372−377.

(10) Yu, Y.; Li, C.; Liu, Y.; Su, L.; Zhang, Y.; Cao, L. Controlled Scalable Synthesis of Uniform, High-Quality Monolayer and Few-Layer MoS_2 Films. *Sci. Rep.* **2013**, *3*, 1866.

(11) Tan, M.; Wang, Z.; Peng, J.; Jin, X. Facile Synthesis of Large and This TiS2 Sheets via a Gas/Molten Salt Interface Reaction. *J. Am. Ceram. Soc.* **2015**, *98*, 1423−1428.

(12) Berkdemir, A.; Gutiérrez, H. R.; Botello-Méndez, A. R.; Perea-López, N.; Elías, A. L.; Chia, C.-I.; Wang, B.; Crespi, V. H.; López-Urías, F.; Charlier, J.-C.; et al. Identification of Individual and Few Layers of WS2 Using Raman Spectroscopy. *Sci. Rep.* **2013**, *3*, 1755.

(13) Anasori, B.; Xie, Y.; Beidaghi, M.; Lu, J.; Hosler, B. C.; Hultman, L.; Kent, P. R.; Gogotsi, Y.; Barsoum, M. W. Two-Dimensional, Ordered, Double Transition Metals Carbides (MXenes). *ACS Nano* **2015**, *9*, 9507−9516.

(14) Özçelik, V. O.; Aktürk, O. Ü.; Durgun, E.; Ciraci, S. Prediction of a two-dimensional crystalline structure of nitrogen atoms. *Phys. Rev. B: Condens. Matter Mater. Phys.* **2015**, *92*, 125420.

(15) Liu, H.; Neal, A. T.; Zhu, Z.; Luo, Z.; Xu, X.; Tomanek, D.; Ye, P. D. Phosphorene: An Unexplored 2D Semiconductor with a High Hole Mobility. *ACS Nano* **2014**, *8*, 4033−4041.

(16) Kamal, C.; Ezawa, M. Two-dimensional buckled and puckered honeycomb arsenic systems. *Phys. Rev. B: Condens. Matter Mater. Phys.* **2015**, *91*, 085423.

(17) Wang, R.; Pandey, G.; Karna, S. P. Atomically Thin Group V Elemental Films: Theoretical Investigations of Antimonene Allotropes. *ACS Appl. Mater. Interfaces* **2015**, *7*, 11490−11496.

(18) Şahin, H.; Cahangirov, S.; Topsakal, M.; Bekaroglu, E.; Aktürk, E.; Senger, R. T.; Çıracı, S. Monolayer Honeycomb Structures of Group-IV Elements and III-V Binary Compounds: First-Principles Calculations. *Phys. Rev. B: Condens. Matter Mater. Phys.* **2009**, *80*, 155453.

(19) Zheng, H.; Li, X.-B.; Chen, N.-K.; Xie, S.-Y.; Tian, W. Q.; Chen, Y.; Xia, H.; Zhang, S. B.; Sun, H. B. Monolayer II-VI semiconductors: A first-principles prediction. *Phys. Rev. B: Condens. Matter Mater. Phys.* **2015**, *92*, 115307.

(20) Yang, S.; Li, Y.; Wang, X.; Huo, N.; Xia, J.-B.; Li, S.-S.; Li, J. High performance few-layer GaS photodetector and its unique photo-response in different gas environments. *Nanoscale* **2014**, *6*, 2582−2587.

(21) Harvey, A.; Backes, C.; Gholamvand, Z.; Hanlon, D.; McAteer, D.; Nerl, H. C.; McGuire, E.; Seral-Ascaso, A.; Ramasse, Q. M.; McEvoy, N.; et al. Preparation of Gallium Sulfide Nanosheets by

DOI: 10.1021/acs.jpcc.6b10334
J. Phys. Chem. C 2017, 121, 4583−4592

Liquid Exfoliation and Their Application As Hydrogen Evolution Catalysts. *Chem. Mater.* **2015**, *27*, 3483−3493.
(22) Lei, S.; Ge, L.; Liu, Z.; Najmaei, S.; Shi, G.; You, G.; Lou, J.; Vajtai, R.; Ajayan, P. M. Synthesis and Photoresponse of Large GaSe Atomic Layers. *Nano Lett.* **2013**, *13*, 2777−2781.
(23) Kamal, C.; Chakrabarti, A.; Ezawa, M. Direct band gaps in group IV-VI monolayer materials: Binary counterparts of phosphorene. *Phys. Rev. B: Condens. Matter Mater. Phys.* **2016**, *93*, 125428.
(24) Mak, K. F.; Lee, C.; Hone, J.; Shan, J.; Heinz, T. F. Atomically Thin MoS2: A New Direct-Gap Semiconductor. *Phys. Rev. Lett.* **2010**, *105*, 136805.
(25) Dai, J.; Zeng, X. C. Bilayer Phosphorene: Effect of Stacking Order on Bandgap and Its Potential Applications in Thin-Film Solar Cells. *J. Phys. Chem. Lett.* **2014**, *5*, 1289−1293.
(26) Xie, M.; Zhang, S.; Cai, B.; Zhu, A.; Zou, Y.; Zeng, H. Two-Dimensional BX (X = P, As, Sb) Semiconductors with Mobilities Approaching Graphene. *Nanoscale* **2016**, *8*, 13407−13413.
(27) Radisavljevic, B.; Radenovic, A.; Brivio, J.; Giacometti, V.; Kis, A. Single Layer MoS2 Transistors. *Nat. Nanotechnol.* **2011**, *6*, 147−150.
(28) Schmidt, H.; Wang, S.; Chu, L.; Toh, M.; Kumar, R.; Zhao, W.; Castro Neto, A.; Martin, J.; Adam, S.; Özyı lmaz, B.; et al. Transport Properties of Monolayer MoS2 Grown by Chemical Vapor Deposition. *Nano Lett.* **2014**, *14*, 1909−1913.
(29) Tsipas, P.; Kassavetis, S.; Tsoutsou, D.; Xenogiannopoulou, E.; Golias, E.; Giamini, S.; Grazianetti, C.; Chiappe, D.; Molle, A.; Fanciulli, M.; et al. Evidence for Graphite-Like Hexagonal AlN Nanosheets Epitaxially Grown on Single Crystal Ag(111). *Appl. Phys. Lett.* **2013**, *103*, 251605.
(30) Al Balushi, Z. Y.; Wang, K.; Ghosh, R. K.; Vila, R. A.; Eichfeld, S. M.; Caldwell, J. D.; Qin, X.; Lin, Y.-C.; DeSario, P. A.; Stone, G. Two-Dimensional Gallium Nitride Realized via Graphene Encapsulation. *Nat. Mater.* **2016**, *15*, 1166.
(31) Wang, S.-f.; Wu, X.-j. First-Principles Study on Electronic and Optical Properties of Graphene-Like Boron Phosphide Sheets. *Chin. J. Chem. Phys.* **2015**, *28*, 588−594.
(32) Schwierz, F.; Pezoldt, J.; Granzner, R. Two-Dimensional Materials and Their Prospects in Transistor Electronics. *Nanoscale* **2015**, *7*, 8261−8283.
(33) Ferrari, A. C.; Bonaccorso, F.; Fal'ko, V.; Novoselov, K.; Roche, S.; Boggild, P.; Borini, S.; Koppens, F. H. L.; Palermo, V.; Ballerini, L.; et al. Science and Technology Roadmap for Graphene Related Two-Dimensional Crystals, and Hybrid Systems. *Nanoscale* **2015**, *7*, 4598−4811.
(34) Castellanos-Gomez, A. Black Phosphorous: Narrow Gap, Wide Applications. *J. Phys. Chem. Lett.* **2015**, *6*, 4280−4291.
(35) López-Castillo, A. Prediction of Boron-Phosphorous Nanographene-Like Material. *Int. J. Quantum Chem.* **2012**, *112*, 3152−3157.
(36) Çakır, D.; Kecik, D.; Şahin, H.; Durgun, E.; Peeters, F. M. Realization of a p-n Junction in a Single Layer Boron-Phosphide. *Phys. Chem. Chem. Phys.* **2015**, *17*, 13013−13020.
(37) Ersan, F.; Aktürk, E.; Ciraci, S. Interaction of Adatoms and Molecules with Single-Layer Arsenene Phases. *J. Phys. Chem. C* **2016**, *120*, 14345−14355.
(38) Üzengi Aktürk, O. Ü.; Aktürk, E.; Ciraci, S. Effects of Adatoms and Physisorbed Molecules on the Physical Properties of Antimonene. *Phys. Rev. B: Condens. Matter Mater. Phys.* **2016**, *93*, 035450.
(39) Özçelik, V. O.; Kecik, D.; Durgun, E.; Çıracı, S. Adsorption of Group IV Elements on Graphene, Silicene, Germanene, and Stanene: Dumbbell Formation. *J. Phys. Chem. C* **2015**, *119*, 845−853.
(40) Kohn, W.; Sham, L. J. Self-Consistent Equations Including Exchange and Correlation Effects. *Phys. Rev.* **1965**, *140*, A1133−A1138.
(41) Hohenberg, P.; Kohn, W. Inhomogeneous Electron Gas. *Phys. Rev.* **1964**, *136*, B864−B871.
(42) Kresse, G.; Furthmüller, J. Efficient Iterative Schemes for Ab-Initio Total-Energy Calculations Using a Plane-Wave Basis set. *Phys. Rev. B: Condens. Matter Mater. Phys.* **1996**, *54*, 11169−11186.
(43) Perdew, J. P.; Burke, K.; Ernzerhof, M. Generalized Gradient Approximation Made Simple. *Phys. Rev. Lett.* **1996**, *77*, 3865−3868.
(44) Gao, W.; Tkatchenko, A. Electronic Structure and van der Waals Interactions in the Stability and Mobility of Point Defects in Semiconductors. *Phys. Rev. Lett.* **2013**, *111*, 045501.
(45) Grimme, S. Semiempirical GGA-type Density Functional Constructed with a Long-Range Dispersion Correction. *J. Comput. Chem.* **2006**, *27*, 1787−1799.
(46) Paier, J.; Marsman, M.; Hummer, K.; Kresse, G.; Gerber, I. C.; Ángyán, J. G. Screened Hybrid Density Functionals Applied to Solids. *J. Chem. Phys.* **2006**, *124*, 154709.
(47) Bianco, E.; Butler, S.; Jiang, S.; Restrepo, O. D.; Windl, W.; Goldberger, J. E. Stability and Exfoliation of Germanane: A Germanium Graphane Analogue. *ACS Nano* **2013**, *7*, 4414−4421.
(48) Cai, Y.; Zhang, G.; Zhang, Y.-W. Layer-dependent Band Alignment and Work Function of Few-Layer Phosphorene. *Sci. Rep.* **2014**, *4*, 6677−6683.
(49) Monkhorst, H. J.; Pack, J. D. Special Points for Brillouin-Zone Integrations. *Phys. Rev. B* **1976**, *13*, 5188.
(50) Togo, A.; Tanaka, I. First Principles Phonon Calculations in Materials Science. *Scr. Mater.* **2015**, *108*, 1−5.
(51) Gonze, X.; Lee, C. Dynamical Matrices, Born Efective Charges, Dielectric Permittivity Tensors, and Interatomic Force Constants from Density-functional Perturbation Theory. *Phys. Rev. B: Condens. Matter Mater. Phys.* **1997**, *55*, 10355−10367.
(52) Togo, A.; Oba, F.; Tanaka, I. First-principles Calculations of the Ferroelastic Transition Between Rutile-type and CaCl2-type SiO2 at High Pressures. *Phys. Rev. B: Condens. Matter Mater. Phys.* **2008**, *78*, 134106.
(53) Özçelik, V. O.; Durgun, E.; Çıracı, S. New Phases of Germanene. *J. Phys. Chem. Lett.* **2014**, *5*, 2694−2699.
(54) Tang, P.; Chen, P.; Cao, W.; Huang, H.; Cahangirov, S.; Xian, L.; Xu, Y.; Zhang, S.-C.; Duan, W.; Rubio, A. Stable Two-dimensional Dumbbell Stanene: A Quantum Spin Hall Insulator. *Phys. Rev. B: Condens. Matter Mater. Phys.* **2014**, *90*, 121408.
(55) E_g(IM) can also be calculated with respect to VBM for holes, but in this study, n-type and p-type doping is not clear for every cases. In this consideration, we calculated E_g(IM) with respect to CBM for all cases, which allows us to make comparisons.
(56) Hashibon, A.; Elsässer, C. First-Principles Density Functional Theory Study of Native Point Defects in Bi_2Te_3. *Phys. Rev. B: Condens. Matter Mater. Phys.* **2011**, *84*, 144117.
(57) Heremans, J. P.; Wiendlocha, B.; Chamoire, A. M. Resonant Levels in Bulk Thermoelectric Semiconductors. *Energy Environ. Sci.* **2012**, *5*, 5510−5530.
(58) Liu, Z.; Yi, X.; Yu, Z.; Yuan, G.; Liu, Y.; Wang, J.; Li, J.; Lu, N.; Ferguson, I.; Zhang, Y. Impurity Resonant States p-type Doping in Wide-Band-Gap Nitrides. *Sci. Rep.* **2016**, *6*, 19537.
(59) Stroppa, A.; Kresse, G. Unraveling the Jahn-Teller Effect in Mn-Doped GaN Using the Heyd-Scuseria-Ernzerhof Hybrid Functional. *Phys. Rev. B: Condens. Matter Mater. Phys.* **2009**, *79*, 201201.
(60) Luo, X.; Martin, R. M. Jahn-Teller Distortion and Ferromagnetism in the Dilute Magnetic Semiconductors GaAs:Mn and Cubic GaN:Mn. *Phys. Rev. B: Condens. Matter Mater. Phys.* **2005**, *72*, 035212.
(61) Chowdhury, C.; Jahiruddin, S.; Datta, A. Pseudo-Jahn-Teller Distortion in Two-Dimensional Phosphorous: Origin of Black and Blue Phases of Phosphorene and Band Gap Modulation by Molecular Charge Transfer. *J. Phys. Chem. Lett.* **2016**, *7*, 1288−1297.

DOI: 10.1021/acs.jpcc.6b10334
J. Phys. Chem. C 2017, 121, 4583−4592